

Asteroid family identification using the Hierarchical Clustering Method and WISE/NEOWISE physical properties

Joseph R. Masiero¹, A. K. Mainzer¹, J. M. Bauer^{1,2}, T. Grav³, C. R. Nugent⁴, R. Stevenson¹

ABSTRACT

Using albedos from WISE/NEOWISE to separate distinct albedo groups within the Main Belt asteroids, we apply the Hierarchical Clustering Method to these subpopulations and identify dynamically associated clusters of asteroids. While this survey is limited to the $\sim 35\%$ of known Main Belt asteroids that were detected by NEOWISE, we present the families linked from these objects as higher confidence associations than can be obtained from dynamical linking alone. We find that over one-third of the observed population of the Main Belt is represented in the high-confidence cores of dynamical families. The albedo distribution of family members differs significantly from the albedo distribution of background objects in the same region of the Main Belt, however interpretation of this effect is complicated by the incomplete identification of lower-confidence family members. In total we link 38298 asteroids into 76 distinct families. This work represents a critical step necessary to debias the albedo and size distributions of asteroids in the Main Belt and understand the formation and history of small bodies in our Solar system.

1. Introduction

In the first publication in this series (Masiero *et al.* 2011, hereafter: Mas11) we presented the preliminary results for Main Belt asteroids (MBAs) from the Wide-field Infrared Survey Explorer (WISE) thermal infrared all-sky survey (Wright *et al.* 2010) and the NEOWISE Solar system enhancement to the core WISE mission (Mainzer *et al.* 2011a). Mas11 also presented the observed albedo and diameter distributions for asteroid families drawn from the overlap between the set of objects detected by NEOWISE and the families identified by Nesvorný (2012) using the Hierarchical Clustering Method (HCM, Zappalà *et al.* 1990, 1994, 1995; Benjoya & Zappalà 2002). In this paper we perform new analysis of the Main Belt using HCM, taking into account dynamical associations as well as asteroid albedo and diameter. This method allows us to incorporate two unique

¹Jet Propulsion Laboratory/Caltech, 4800 Oak Grove Dr., MS 183-601, Pasadena, CA 91109, Joseph.Masiero@jpl.nasa.gov; amainzer@jpl.nasa.gov; James.Bauer@jpl.nasa.gov; Rachel.Stevenson@jpl.nasa.gov

²Infrared Processing and Analysis Center, Caltech, Pasadena, CA

³Planetary Science Institute, Tucson, AZ tgrav@psi.edu

⁴Department of Earth and Space Sciences, University of California, Los Angeles, CA cnugent@ucla.edu

characteristics of asteroid families that both result from an origin in a catastrophic disruption of a single parent: compositional consistency and minimal orbital velocity differences.

Asteroid families were first identified as groups of objects that clustered tightly in orbital element-space by Hirayama (1918) nearly a century ago. Subsequent work has confirmed that families originate from the catastrophic breakup of a single parent asteroid after an impact (see Cellino *et al.* 2009, for a recent review of the current state of the field). This single mineralogical origin causes families to cluster tightly not only when comparing orbital elements but also when investigating colors (Ivezić *et al.* 2002; Parker *et al.* 2008), reflectance spectra (e.g. Binzel & Xu 1993; Cellino *et al.* 2001) and albedo (Mas11). We note that while the asteroid (4) Vesta shows an albedo range of 0.10–0.67 across its surface (Reddy *et al.* 2012), and thus any other differentiated asteroid may have similar large variation, the Vesta asteroid family has a albedo distribution comparable in width to other asteroid families (Mas11).

Building further on the origin of families as a result of collisionally-driven breakups, the size-frequency distribution (SFD) of asteroid family members acts as a tracer of the physical properties of the original parent body and can even be used to constrain the impact velocity and angle (Zappalà *et al.* 2002; Durda *et al.* 2007). However, a major deficiency in the field to date has been the lack of measured diameters for the family members, forcing these values to be estimated based on the apparent visible magnitude of the object. Furthermore, the strong selection effects imposed by visible light surveys against the discovery of low albedo objects (particularly the smallest low albedo objects) results in a skew in the size distributions of linked families. Albedo measurements of the largest bodies in a family are often available from the Infrared Astronomical Satellite (*IRAS*) data set (Tedesco *et al.* 2002) and can be used to assume an albedo for all family members, but this can add a significant and systematic error to the diameters, especially in the cases where it is unclear if the largest body in a family is indeed associated with the other members (e.g. Cellino *et al.* 2001; Masiero *et al.* 2012b). From the NEOWISE survey we now have measurements of diameters for over 130,000 Main Belt asteroids with relative errors of $\sim 10\%$ (see Mas11 and Mainzer *et al.* 2011b). Using this new data set along with the associated proper orbital elements for these objects, we identify the high-confidence associations of asteroid families detected by NEOWISE.

2. Data

Proper orbital elements, which are key to the determination of asteroid family membership, are the time averaged values of the semimajor axis, eccentricity, and inclination after removing the short-period perturbations by Jupiter and Saturn and averaging over long-period variations (Milani & Knežević 1998). Proper elements are preferred to osculating elements for family identification as they are stable over long time periods, and thus asteroid families cluster more tightly in proper orbital element-space (Carpino *et al.* 1986). We use the proper orbital elements computed following

Milani & Knežević (1994, 1998) that are provided on the AstDys website¹ to identify asteroid families in this work.

There are two primary methods for determining proper elements: analytic and synthetic. Using the analytic method, a Fourier expansion of the Hamiltonian is solved for directly. Conversely the synthetic method integrates the present day osculating orbits using numerical simulations and determines the proper elements from that evolution over time. While the analytic method produces more accurate results, it has a fundamental limit of $\sim 18^\circ$ inclination above which the solutions degrade due to the truncation of the Hamiltonian that is typically employed (Milani & Knežević 1994). As NEOWISE observed the entire sky, it detected and discovered over 15000 objects at inclinations $> 18^\circ$, over ten percent of our total sample. In order to consider all asteroids detected by NEOWISE we use the synthetic proper elements for this work. This allows us to have the maximum sample size however synthetic proper elements have their own inherent limitations: oscillations with periods much longer than the integration time (typically ~ 10 million years) will not be removed properly and the forest of weak secular resonances in the Main Belt can result in chaotic cases that show up as banding in the structure of the semimajor axis distribution (Knežević & Milani 2000).

Following the methods of (Knežević & Milani 2000) we have integrated the orbits of all Main Belt asteroids that were detected by NEOWISE and have measured diameters and albedos, but not represented in the AstDys catalog. This will include objects with very short arcs, in particular those discovered by NEOWISE that have had minimal ground-based followup and thus do not have measured orbits with sufficient quality to accurately integrate their positions over millions of years. We include these for completeness, but with the appropriate caveats for our results.

We draw our physical properties for Main Belt asteroids primarily from the measurements made by the WISE spacecraft as part of the NEOWISE project. We include in our analysis MBAs that were detected and discovered throughout the entire mission, both the cryogenic and post-cryogenic surveys (Mainzer *et al.* 2011a, 2012). WISE surveyed the sky simultaneously in four thermal infrared bands ($3.4 \mu\text{m}$, $4.6 \mu\text{m}$, $12 \mu\text{m}$, and $22 \mu\text{m}$) from a polar low-Earth orbit, progressing one degree per day. WISE imaged the entire static sky over the course of 6 months starting 14 January 2010, and began a second pass survey until the exhaustion of the outer cryogen tank on 6 August 2010. At this point, the longest wavelength channel was lost and WISE carried out a 3-Band Cryo survey until 29 September 2010 when the inner cryogen tank was exhausted. The NEOWISE Post-Cryo Survey to complete coverage of the largest MBAs and discover new near-Earth objects began 30 September 2010 and ended on 1 February 2011, using only the two shortest wavelength bands. All phases of the mission employed the WISE Moving Object Processing System (WMOPS) to detect moving objects in the Level 1 WISE images. WMOPS required a minimum of 5 detections to link a track (although a typical track had 10 – 12 detections), which was then submitted to the Minor Planet Center (MPC) for further verification. In total, WMOPS detected $> 158,000$ solar system objects, the majority of which were MBAs.

¹<http://hamilton.dm.unipi.it/astdys/index.php>

Diameters and albedos for MBAs seen during the Fully Cryogenic survey were given in Mas11, while physical properties for objects detected in the 3-Band Cryo and Post-Cryo Surveys were presented in Masiero *et al.* (2012a). We also include diameters and albedo measured for 150 objects by the IRAS mission (Tedesco *et al.* 2002). In most cases these objects were so large that they saturated in the WISE images, though a small number were missed due to the exhaustion of cryogen, observing geometry effects, background contamination, or other filtering in the WISE or NEOWISE data processing pipelines. When these data are combined with the synthetic proper orbital elements our total sample size is 112,286 MBAs, which we use for the study presented here. We note that this is smaller than the total number of objects detected by NEOWISE due to the fact that $\sim 24,000$ objects do not have stable proper orbital element solutions. Nearly three quarters of the unstable objects have observational arcs shorter than one month implying that their orbits are not well known and thus their proper elements cannot be reliably computed. The remaining ~ 6000 unstable objects have orbital elements that are indistinguishable from other MBAs, and orbital arcs typically of one year or more. We note that only nine of these objects have received number designations, and thus the provisional orbits may still be uncertain, which could result in non-converging proper elements. Strangely, we also find that low albedo objects dominate these long-arc unstable MBAs ($\sim 90\%$ have albedos of $p_V < 0.11$), which is much larger than the fraction of low albedo objects in any of the regions of the Main Belt (Mas11). Albedo is not considered when calculating asteroid proper elements and thus should not affect these results, however low albedo objects are more likely to be fainter than a high albedo object during a given observation epoch. Thus we may be seeing low signal-to-noise uncertainties in a number of individual observations propagating into the final orbits. Conversely, these objects may indeed be unstable and thus transitional in their current orbits, potentially representing low albedo objects from more distant regions of the Solar system that have been implanted in the Main Belt. Distinguishing between these two possibilities, however, is beyond the scope of the current work and will be the subject of future investigation.

We show in Figure 1 the distribution of albedo as a function of diameter for all objects used in this work. Two populations are apparent, a low-albedo population at $p_V \sim 0.06$ and a high-albedo population at $p_V \sim 0.25$ (c.f. Mas11). The low-albedo population is shifted to larger diameters compared to the high-albedo population due to selection biases in optical catalogs. While the sensitivity of NEOWISE was effectively albedo-independent (Mainzer *et al.* 2011d; Grav *et al.* 2011a,b), followup observations of NEOWISE discoveries by ground-based optical surveys suffer from a decreased sensitivity to smaller, lower albedo asteroids. This will result in the apparent shift in the low albedo population to larger diameters. Though we assume for purposes of this analysis that families have uniform albedos, this bias means that the derived membership lists for lower albedo families will be missing more small members than would a high albedo family in the same region of the Main Belt.

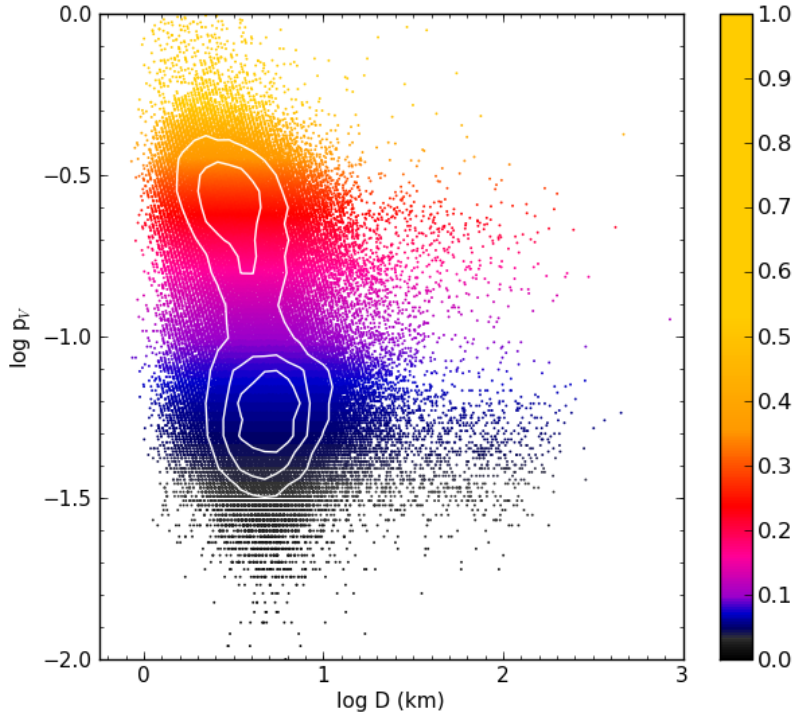


Fig. 1.— Asteroid albedo (p_V) vs diameter for the 112,286 MBAs used in this work. The color of the points also indicates albedo, as given in the color bar. The white contours indicate the density of points in the saturated regions. Two albedo components are apparent, with the shift in the low albedo distribution to larger diameters a result of the selection bias against small, dark objects in optical observations. The horizontal picket fence effect at low albedos is an artifact of the precision of the quoted albedos. The subtle diagonal linear trends at small ($D < 2$ km) diameters are an artifact of the precision of the literature H absolute magnitudes. Albedos larger than ~ 0.5 are likely artifacts of bad H or G values (c.f. Pravec *et al.* 2012)

Recently, Pravec *et al.* (2012) have presented evidence of possible biases in the various catalogs of asteroid absolute magnitudes (H), and they highlight the effect that these biases have on the albedo values derived for a small sample NEOWISE-observed MBAs. While it is clear that in many cases the published absolute magnitudes do not reflect the true values when measured independently, these deviations show a non-linear relationship, with a maximal deviation at $H \sim 14$ mag. Additionally, the scatter in magnitude difference at $H > 6$ mag is large, and almost always comparable to the mean of the differences. As such, we chose not to implement a blanket offset correction to the catalog H values, which would tend to offset the NEOWISE-derived albedos. We note that diameters derived from thermal infrared measurements are largely unaffected by offsets in H , and quoted albedo errors include estimated uncertainties on H and G of 0.3 and 0.1 respectively. Large

surveys recently begun or soon to come online (e.g. Pan-STARRS, LSST) should greatly improve the H catalog values for most asteroids. Additionally, implementation of the $H-G_1-G_2$ magnitude phase function Muinonen *et al.* (2010) may also improve the determined albedos for cases where there is sufficient photometric data. For this work, we use the albedos as published that are derived from the literature H magnitudes, but with appropriate error bars. Future work will revise the catalog of NEOWISE-measured diameters and albedos using the updated NEOWISE science data processing system and the most current values of H .

3. Hierarchical Clustering Method

Asteroid families were originally identified as pairs or groups of objects with orbital elements that clustered more tightly than would otherwise be expected from a random distribution of objects. Zappalà *et al.* (1990) present a method for association of asteroid families based on their proper orbital elements called the Hierarchical Clustering Method (HCM) which uses a distance function and a velocity cut to link objects together into clusters. Iterating over each body in the population, the distance between it and all other asteroids is calculated by converting the difference in orbital elements into a pseudo-velocity. All objects within a given velocity threshold are added into the family. Each family member is then similarly tested, accreting nearby objects into the family, until no further objects are added. The selected velocity cutoff will strongly dictate the size of the family and the reliability of the associations: a cutoff velocity that is too low will only identify the core regions of the densest families, while a cutoff velocity that is too large will include a large number of interlopers in the family lists or accept spurious groupings of objects that do not have a real collisional origin.

Following Zappalà *et al.* (1994), we apply a distance metric of

$$d = 2\pi F \sqrt{\frac{\frac{5}{4} \left(\frac{a_i - a_c}{a_c}\right)^2 + 2(ecc_i - ecc_c)^2 + 2(\sin inc_i - \sin inc_c)^2}{a_c}}$$

where d is the distance in m/s between the objects, F is the conversion factor changing AU/yr to m/s, a , ecc , and inc are the proper semimajor axis, eccentricity, and inclination of the body, and the subscripts c and i indicate the center body and the body being tested, respectively. We perform HCM analysis on every object in our MBA sample, at velocity limits ranging from 5 m/s to 200 m/s in steps of 5 m/s. This allows us to build up a database of all associations for each object at a range of velocities.

Following Nesvorný (2012) we divide the Main Belt into three regions separated by strong Jupiter mean motion resonances: the inner Main Belt (IMB, $1.8 < a < 2.5$ AU), the middle Main Belt (MMB, $2.5 < a < 2.82$ AU), and the outer Main Belt (OMB, $2.82 < a < 3.6$ AU). We set a limit on perihelion distance of $q > 1.666$ AU to ensure Mars-crossing asteroids are not included in our data set. We use physical properties as a discriminant in family identification by dividing each

region of the Belt into two groups by albedo. While the majority of MBAs show a bimodal albedo distribution (Figure 1), a small number of asteroid families have a mean albedo that falls in between these two peaks (Mas11). In order to ensure that these families can be properly identified and that the wings of the albedo distribution of each family are not truncated, we have separated the regions by albedo allowing for an overlap region in between. As such, objects with moderate albedo will appear in both lists. Our high albedo group for each Main Belt region includes all objects with $p_V > 0.065$ while the low albedo group includes objects with $p_V < 0.155$, which represents a buffer of $\pm 40\%$ relative to the central minimum reflectance of the MBA albedo distribution at $p_V = 0.11$ (Mas11). The total number of objects in each group searched as well as the bounding semimajor axes and albedo are shown in Table 1.

Table 1: Main Belt regions used for HCM analysis

Region	Semimajor Axis Range (AU)	Albedo Range	Number [†]	QRL [‡] (m/s)
IMB _{high}	$1.8 < a < 2.5$	$p_V > 0.065$	21013	110 ± 6
IMB _{low}	$1.8 < a < 2.5$	$p_V < 0.155$	10622	132 ± 7
MMB _{high}	$2.5 < a < 2.82$	$p_V > 0.065$	26214	101 ± 8
MMB _{low}	$2.5 < a < 2.82$	$p_V < 0.155$	22958	102 ± 7
OMB _{high}	$2.82 < a < 3.6$	$p_V > 0.065$	24204	102 ± 7
OMB _{low}	$2.82 < a < 3.6$	$p_V < 0.155$	38691	107 ± 8

[†]Summed number of objects in all regions is greater than total population due to overlap between albedos; see text for details

[‡]Quasi-Random Level used for determining significant family linkages

To enable rapid searching of each region investigated we employ a k-dimensional (KD)-tree query to perform an initial reduction in the possible associations for each object. KD-trees are computational methods of dividing up multidimensional data to increase the efficiency of searches for specific data points within that space. All objects identified by the KD-tree test are then compared to the velocity limit of that run to test for family membership. This process provides a dramatic reduction in run time of the search procedure.

After identifying the family associations at each velocity cut for each region of the Belt, we need to determine which velocity cut represents the optimal blend between completeness and accuracy. We follow Zappalà *et al.* (1994) and use a Quasi-Random Level (QRL) test to determine at which point background objects begin to become a significant contributor to family lists. The methodology behind a QRL test is to construct a synthetic population based on the orbital elements of the real MBAs and determine at which velocity limit the synthetic objects begin to be linked by HCM. This velocity can then be considered the level at which a quasi-random population of objects begin to contribute to family lists; any linkages below this limit are unlikely to be random associations. We note that as the overall population of known MBAs grows, the average distance between any two asteroids will decrease and thus the QRL will get smaller over time (although as more family members are observed the velocity cut at which they link will also shrink). We use a lower limit of ten objects as the minimum size group we consider both for family membership and QRL determination.

In order to construct a representative synthetic background population, one must know which objects are in the background as opposed to belonging to a family and thus *a priori* have a list of known family members. This becomes especially critical when a large, dense family dominates a small area of the phase space. If these families are not removed, the QRL will be made artificially smaller as real family members begin to link together in the quasi-random population.

Removing a too many objects will decrease the number density and thus increase the calculated QRL, while removing too few will have the opposite effect. Similarly, replacing removed objects with randomly generated ones will artificially increase the number of objects not associated with families when compared to the real population, causing them to link at a lower level than the observed background. The two parameters determining the number of objects removed are the linking velocity level chosen and the size of the smallest family removed. By varying these two parameters, we tested their effect on the final QRL determination for all regions of the Main Belt. We find that the size of the smallest family removed (from 50 – 200 members) has only a minimal effect on the determined QRL, as it is the few largest families that dominate the artificially reduced QRL levels. On the other hand, the velocity level chosen (from 75 – 150 m/s) does have a strong effect on the final determined QRL, which track each other closely. We use the lists of members of the largest families identified by Nesvorný (2012) to find a velocity cut in our determination that most closely reproduces those families, and use that velocity level as the limit for large family removal.

In this implementation we use limits of 100 members and a velocity cut of 125 m/s to remove the largest families. Any asteroid in one of these families was removed from the sample used to generate the quasi-random population. We then divided each region into subregions by semimajor axis so that each eccentricity-inclination slice contained 10% of the total number of objects in the entire region. The quasi-random population was built by randomly drawing *a*, *ecc*, and *inc* values from the members of the slice. This ensured that the distribution of these three orbital parameters remained identical for the original and quasi-random populations, minus the removed large families. The slices were then reassembled and HCM was run on this population for all velocity cuts from 5 – 200 m/s in steps of 5 m/s. This process was performed ten times for each region of the Main Belt, and the velocity levels of the first five pseudo-families of each trial were averaged to determine the QRL for the region. This provides both a mean QRL level for each region as well as an estimate of the uncertainty on that value, both of which are shown in Table 1.

A common way of representing asteroid families is a ‘stalactite’ plot, which shows the membership of each family as a function of cutoff velocity as well as which families merge or fragment at various cutoff levels. We show stalactite plots for each of the six regions considered here in Figures 2-7. We also show the 1σ range of the QRL as the grey box overlaid on the stalactites. At each velocity step, the families are labeled with the numerical designation of the member with the largest measured diameter. Designations will change with decreasing velocity as objects connected more loosely fall out of the family list. We have left the smallest families on each plot unlabeled to preserve the clarity of the figures.

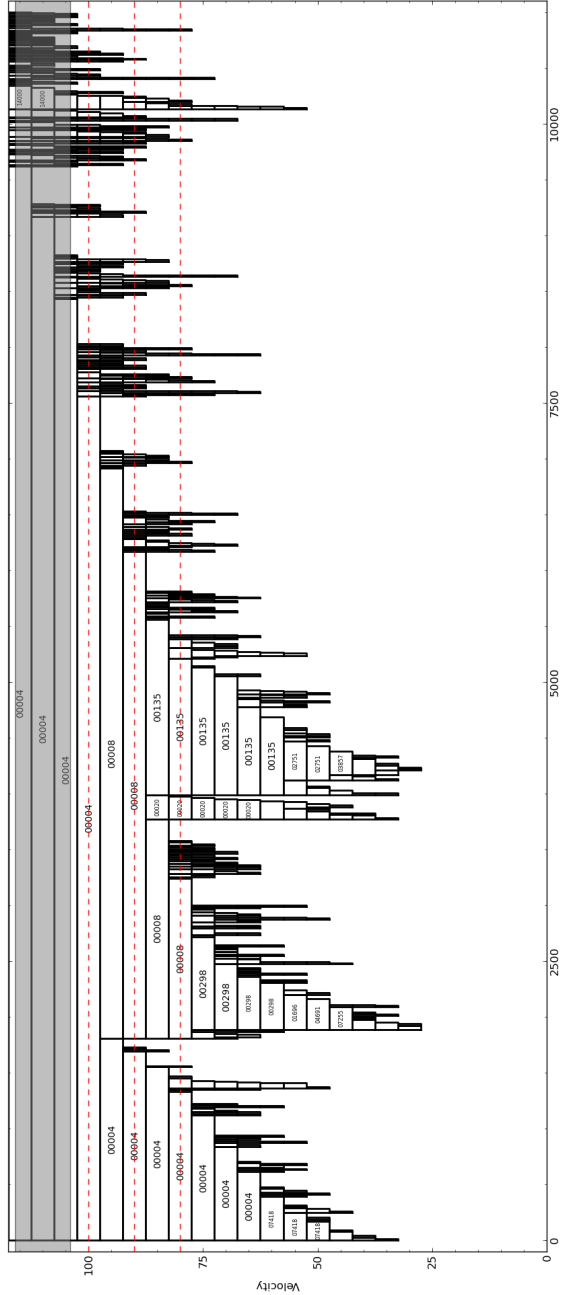


Fig. 2.— Stalactite diagram showing family associations for the high albedo objects in the inner Main Belt. Families are identified by the designation number of the largest asteroid contained in the family list and length of each bar indicates the number of objects contained in that family at that velocity cut. The count at the bottom of the plot is an arbitrary sum of the bars at the topmost level. Small families are left unlabeled for clarity but are discussed in the text. The grey box shows the 1σ range around the QRL level: family associations within this range are likely contaminated by background objects. The three dashed red lines indicate the velocities used to extract family membership lists.

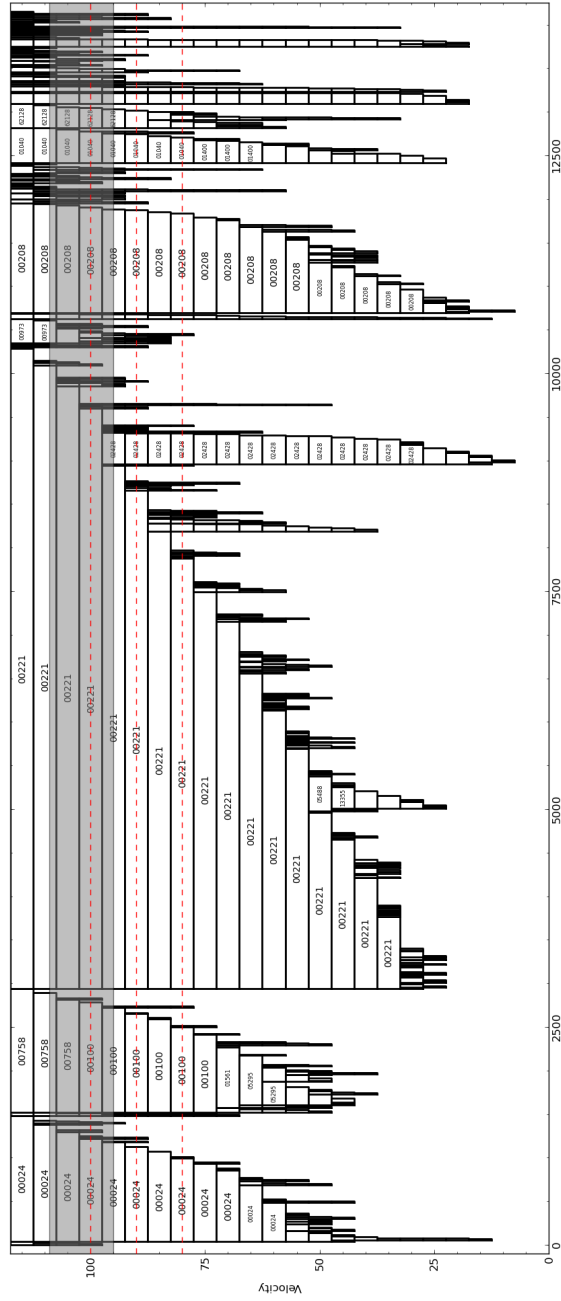


Fig. 6.— The same as Figure 2 but for the high albedo outer Main Belt asteroids.

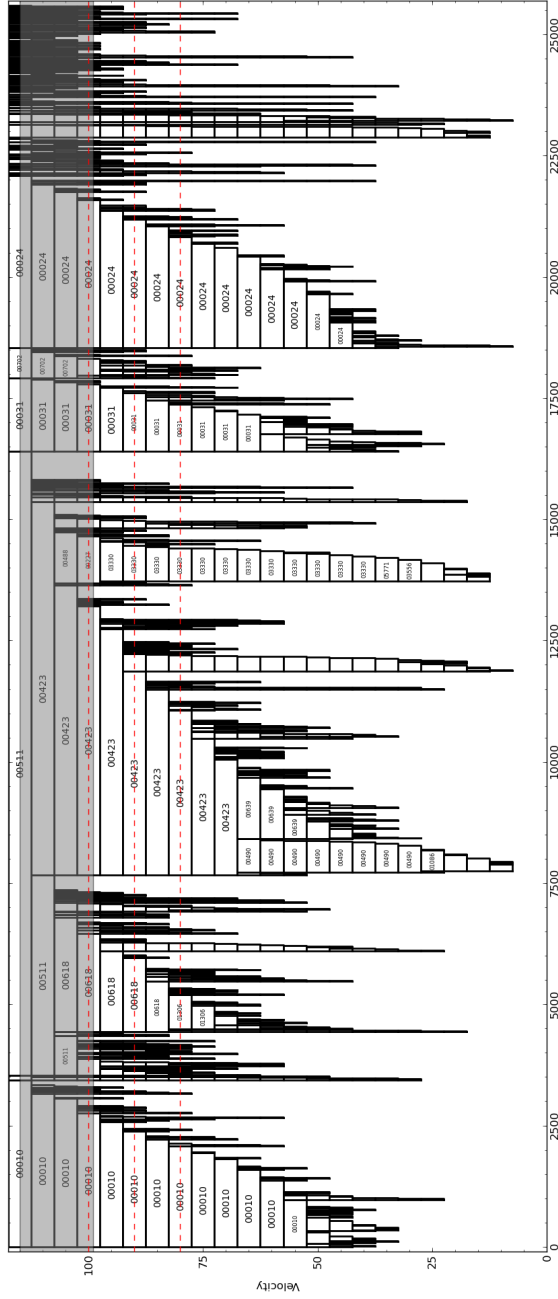


Fig. 7.— The same as Figure 2 but for the low albedo outer Main Belt asteroids.

Stalactite plots are read from top to bottom, showing the least- to most-significant clusters of objects. For example, in Figure 2 we can follow the evolution of the objects linked to (8) Flora. At large velocities ($v_{link} > 100$ m/s) a large fraction of the asteroids in the IMB_{high} region link to (4) Vesta. Even below the QRL level at $v_{link} = 100$ m/s all of the large families remain grouped together. At $v_{link} = 95$ m/s the Vesta and Flora clumps separate, and at $v_{link} = 85$ m/s the Flora clump breaks up into the Flora, (20) Massalia, and (135) Hertha families. At velocities below $v_{link} = 80$ m/s Flora no longer links with the family, and nearly half of the other family members are rejected at this cutoff as well. In contrast, Vesta remains linked to its family down to $v_{link} = 65$ m/s, though this family also loses a substantial fraction of linked members as the cutoff velocity decreases.

4. Results and Discussion

4.1. Identified Families

We use our stalactite plots as a first cut to guide our selection of the optimal cutoff velocity at which to extract each family list. For each region we have extracted families at three different velocity cuts: one at or near the lower edge of the identified QRL zone and two others at 10 m/s and 20 m/s below that level to separate overlapping families (e.g. Vesta and Flora) and winnow out background objects that may be connecting below the QRL level. This is similar to the method employed by Milani *et al.* (2010) to identify the Hungaria family. The extraction levels for each region are indicated in Figures 2-7 by the dashed red lines. We note that due to the assumptions inherent in our QRL determination, some of the associations presented here may be incomplete or even spurious. A more detailed analysis of each family individually can refine these associations, and will be the subject of future work.

By plotting the diameter of each family member against their proper semimajor axis, and color-coding the points to represent albedo, we construct “petal” plots which can be used to diagnose the reliability of the family association. An ideal family will have a large parent body at the bottom-center of the plot with the family spreading to smaller diameters and larger distance in semimajor axis from the parent, as would be expected from a family evolved by Yarkovsky drift (Bottke *et al.* 2006). For families in dense regions of the Main Belt, large families will link together even at levels below the QRL. By choosing a lower velocity cutoff we can disentangle these overlapping families. Figure 8 shows an example of this, where the Massalia family blends with the Flora and Vesta family as the velocity cutoff is increased. We can also use this technique to filter out large background objects that may be linked to a family and thus mis-identified as the parent body. Figure 9 shows an example of this scenario, where (500) Selinur is linked to the family at larger velocities, but at the lowest cutoff is rejected from the family. The albedo of (500) Selinur and its placement on the plots indicate it is unlikely to be the parent of the family, and that (3811) Karma is a much more likely parent body. This results in a family with a very classic petal shape.

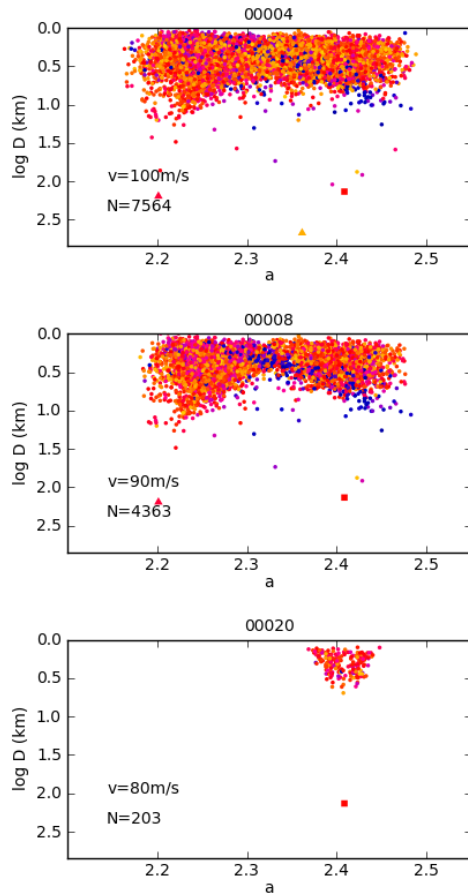


Fig. 8.— Diameter vs proper semimajor axis for the Massalia family at three different cutoff velocities (from top to bottom: 100 m/s, 90 m/s, 80 m/s). The color of each point indicates its albedo as in Figure 1, while N lists the number of objects linked at that cutoff. Each subplot is titled with the largest object included in the family, the presumed parent. Here, the family of (20) Massalia (marked as a square) blends with the families of (8) Flora and (4) Vesta (both marked as triangles) at velocity cutoffs larger than 80 m/s.

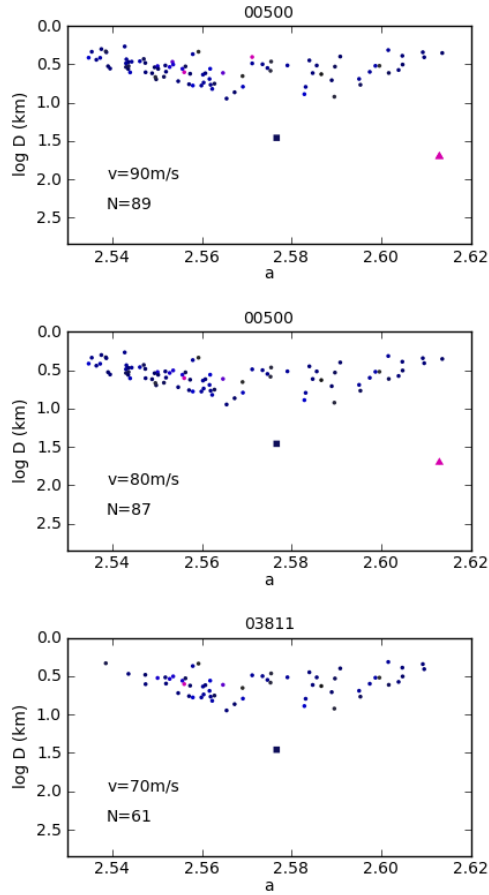


Fig. 9.— Diameter vs proper semimajor axis for the Karma family at three different cutoff velocities (from top to bottom: 90 m/s, 80 m/s, 70 m/s). The color of each point indicates its albedo as in Figure 1, while N lists the number of objects linked at that cutoff. Each subplot is titled with the largest object included in the family, the presumed parent. Here, (500) Selinur (marked as a triangle) links with the family at larger velocities, but is rejected at 70 m/s, making (3811) Karma (marked as a square) the most likely parent.

Using the physical and orbital parameters of the objects that were linked together at each velocity cutoff, we identify the highest reliability families in the Main Belt that can be detected with this technique. To ensure a high level of reliability and measure statistically significant family properties we have only included families with > 40 members. We find 76 families throughout the Main Belt that pass these cutoffs representing 38,298 MBAs (approximately 35% of all objects considered), and another ~ 60 candidate groupings below of 40 member limit that are too small to be definite detections. We give a list of the identified families, with the number (in MPC-packed format) and name of the largest member, the HCM velocity the family was extracted at (v_{link}), the median proper semimajor axis, eccentricity, and inclination for the family (a_{med} , ecc_{med} , inc_{med} , respectively), and the number of linked family members (N) in Table 2. We also include average physical properties for each family in Table 2 (see Section 4.2 for description of these parameters). Names with a ‘*’ suffix indicate cases of ambiguous parent bodies (see below). In Table 3 we present the full list of asteroids associated with families, their orbital and physical parameters, and identify the family to which they have been linked.

Table 2.: Orbital elements, median and maximum diameters, average albedos, and raw SFD slopes (α) for observed asteroid families

Number	Name	v_{link} (m/s)	a_{med} (AU)	ecc_{med}	inc_{med} (deg)	D_{max} (km)	D_{med} (km)	\bar{pV}	σ_{pV}	α_{SFD}	σ_{α}	N
00004	Vesta	80	2.3469	0.0972	6.6786	468.30	2.50	0.361	0.111	-3.448	0.038	1331
00008	Flora	80	2.2543	0.1409	5.4513	155.74	2.70	0.288	0.088	-2.589	0.032	929
00020	Massalia	80	2.4035	0.1636	1.4211	135.68	1.91	0.243	0.066	-3.929	0.164	203
00135	Hertha	80	2.3990	0.1796	2.4243	82.15	2.42	0.284	0.091	-3.375	0.050	1113
00254	Augusta*	90	2.1986	0.1213	4.1490	11.85	2.45	0.305	0.094	-1.727	0.111	72
00434	Hungaria	100	1.9466	0.0771	21.0020	8.93	1.66	0.722	0.156	-2.102	0.397	48
00587	Hypsipyle	100	2.3354	0.2203	24.0667	12.23	3.01	0.318	0.093	-2.285	0.389	43
01646	Rosseland*	100	2.3501	0.0983	8.0594	12.47	3.23	0.194	0.047	-2.393	0.293	46
02409	Chapman	80	2.2746	0.1342	3.2275	8.70	2.31	0.288	0.076	-2.391	0.205	78
04689	Donn	90	2.2763	0.1166	4.7007	6.14	2.72	0.278	0.074	-3.326	0.351	60
13698	13698*	80	2.4368	0.1129	6.3787	5.97	2.75	0.359	0.107	-4.185	0.309	87
00012	Klio*	120	2.3859	0.1922	9.3462	126.64	3.57	0.062	0.019	-2.750	0.082	269
01715	Salli	120	2.4114	0.2289	10.9966	24.16	3.49	0.062	0.021	-2.907	0.103	178
00163	Erigone	120	2.3718	0.2088	5.0486	81.58	2.98	0.051	0.012	-3.229	0.040	1093
00298	Baptistina*	100	2.2737	0.1451	5.6067	21.14	2.34	0.158	0.029	-2.692	0.048	549
00302	Clarissa	120	2.3967	0.1082	2.6910	38.53	3.02	0.056	0.017	-3.242	0.110	228
00554	Polana*	120	2.3566	0.1485	2.8258	102.78	3.11	0.057	0.015	-2.376	0.016	2438
00623	Chimaera	130	2.4456	0.1500	14.8210	44.09	4.16	0.059	0.011	-2.507	0.357	46
00752	Sulamitis	120	2.4407	0.0894	5.0428	60.85	3.38	0.052	0.013	-2.408	0.090	191
00003	Juno	80	2.6654	0.2351	13.3530	246.60	2.15	0.252	0.062	-3.318	0.121	196
00005	Astraea	80	2.5823	0.1986	4.4909	113.00	2.50	0.279	0.072	-2.962	0.178	94
00015	Eunomia	70	2.6214	0.1497	13.1676	299.21	4.07	0.268	0.073	-2.958	0.025	2140
00472	Roma*	80	2.6022	0.0915	14.8032	47.04	3.63	0.257	0.078	-2.147	0.024	712
00480	Hansa	80	2.6557	0.0111	21.9749	65.67	3.12	0.249	0.091	-2.358	0.231	65
00606	Brangane	70	2.5817	0.1803	9.6134	39.53	2.87	0.112	0.034	-3.322	0.354	57
00808	Merxia	80	2.7431	0.1341	5.0083	37.68	3.16	0.229	0.062	-2.624	0.180	90
00847	Agnia	80	2.7902	0.0723	3.8130	30.08	3.84	0.227	0.070	-2.850	0.107	180
01658	Innes	80	2.5799	0.1727	7.5910	13.81	3.05	0.256	0.071	-3.284	0.159	155
02595	Gudiachvili*	80	2.7718	0.1311	9.1140	14.62	3.97	0.265	0.069	-3.087	0.055	584
00539	Pamina	80	2.7428	0.1628	8.2446	56.04	4.57	0.057	0.019	-2.588	0.177	88
01734	Zhongolovich*	80	2.7861	0.1958	7.8512	26.70	4.86	0.054	0.014	-2.557	0.034	903

Table 2:: (continued)

Number	Name	v_{link} (m/s)	a_{med} (AU)	ecc_{med}	inc_{med} (deg)	D_{max} (km)	D_{med} (km)	\overline{pV}	σ_{pV}	α_{SFD}	σ_{α}	N
00145	Adeona	70	2.6513	0.1663	11.6481	132.59	4.46	0.059	0.014	-2.704	0.027	1321
00128	Nemesis	70	2.7343	0.0896	4.8703	193.08	3.64	0.071	0.023	-3.718	0.094	390
00363	Padua	55	2.7344	0.0411	5.3190	86.04	4.15	0.067	0.018	-2.655	0.048	512
00272	Antonia*	55	2.7842	0.0476	4.3932	25.67	4.01	0.046	0.011	-2.966	0.040	861
00144	Vibilia	90	2.6715	0.1888	3.8417	142.38	4.33	0.064	0.013	-3.095	0.123	184
00322	Phaeo	90	2.7875	0.1935	9.4217	73.15	3.37	0.068	0.017	-2.956	0.282	72
00342	Endymion*	70	2.5719	0.1401	8.7950	64.27	3.39	0.043	0.013	-2.812	0.086	230
00396	Aeolia	80	2.7399	0.1678	3.4398	37.29	2.85	0.094	0.027	-2.823	0.289	62
00404	Arsinoe*	80	2.6257	0.2304	13.1558	105.41	4.17	0.051	0.015	-2.391	0.137	113
00410	Chloris	90	2.7458	0.2522	8.7834	118.93	5.33	0.084	0.029	-2.571	0.144	116
03811	Karma	70	2.5690	0.1066	10.7836	28.75	3.96	0.054	0.010	-2.603	0.329	61
00569	Misa	80	2.6479	0.1778	2.2867	78.93	3.46	0.052	0.015	-2.447	0.054	357
01128	Astrid	80	2.7773	0.0484	0.6818	48.63	3.50	0.046	0.011	-2.585	0.083	201
01668	Hanna	80	2.7932	0.1766	4.2265	25.83	3.86	0.051	0.013	-3.608	0.185	122
02669	Shostakovich*	90	2.7687	0.1739	9.2127	16.47	5.14	0.051	0.016	-3.001	0.203	98
03567	Alvema*	90	2.7702	0.2806	8.3054	14.53	4.24	0.056	0.016	-3.302	0.296	62
05079	Brubeck*	90	2.5722	0.2493	12.4977	16.95	4.00	0.066	0.018	-3.011	0.071	441
00208	Lacrimosa*	90	2.8913	0.0489	2.1090	49.99	4.85	0.238	0.062	-2.392	0.024	1175
00179	Klytaemnestra	80	2.9852	0.0674	8.7805	74.59	4.17	0.217	0.075	-5.168	0.606	90
00221	Eos*	90	3.0248	0.0744	10.1660	95.63	4.98	0.157	0.045	-2.320	0.010	5718
01040	Klumpkea	90	3.1230	0.1976	16.8220	22.67	4.08	0.235	0.066	-2.934	0.091	333
03985	Raybatson*	90	2.8516	0.1221	15.0523	22.11	3.54	0.167	0.056	-3.572	0.234	126
00010	Hygiea	100	3.1573	0.1308	5.2384	453.24	5.75	0.068	0.022	-2.484	0.014	2757
00024	Themis	100	3.1371	0.1505	1.3982	193.54	6.88	0.066	0.021	-2.177	0.012	3052
00031	Euphrosyne	100	3.1679	0.1940	26.5578	281.98	6.11	0.056	0.016	-4.404	0.053	1392
00081	Terpsichore	90	2.8866	0.1848	8.1925	123.96	4.68	0.051	0.014	-3.842	0.792	49
00087	Sylvia	90	3.4981	0.0558	9.8460	288.38	7.66	0.056	0.016	-2.624	0.365	60
00096	Aegle	90	3.0570	0.1844	16.5379	177.77	6.63	0.071	0.016	-3.418	0.296	86
03330	Gantrisch	90	3.1466	0.1974	10.1892	37.64	5.51	0.043	0.011	-3.171	0.054	734
00276	Adelheid*	100	3.1953	0.0665	21.8977	100.35	8.76	0.065	0.019	-2.244	0.050	358
00283	Emma	80	3.0508	0.1142	9.0734	145.55	5.74	0.044	0.013	-3.160	0.081	340
00490	Veritas	65	3.1700	0.0615	9.2533	118.80	5.79	0.066	0.020	-2.767	0.044	686
24649	Balaklava*	90	3.1880	0.2108	14.1109	16.79	4.23	0.056	0.011	-2.244	0.148	88
00511	Davida	90	3.1476	0.1903	14.4627	285.84	7.66	0.058	0.018	-1.455	0.068	104
00618	Elfriede	80	3.1886	0.0582	15.8548	131.23	5.16	0.054	0.018	-3.621	0.799	45
01306	Scythia*	80	3.1408	0.0896	16.4274	72.24	6.59	0.057	0.017	-2.482	0.035	705
01303	Luthera	90	3.2169	0.1210	18.7869	102.43	6.81	0.047	0.013	-3.794	0.176	176
00702	Alauda	100	3.2184	0.0183	21.5554	196.47	10.22	0.065	0.015	-1.747	0.197	49
00778	Theobalda	90	3.1745	0.2541	14.3001	55.32	6.04	0.061	0.020	-3.199	0.156	144
00780	Armenia	90	3.1057	0.0690	18.1677	114.26	5.46	0.053	0.014	-4.563	1.482	40
00816	Juliana	90	2.9887	0.1460	13.2853	50.08	5.62	0.042	0.014	-3.260	0.640	42
00845	Naema	90	2.9333	0.0355	11.9642	58.53	5.25	0.059	0.016	-3.955	0.141	246
00928	Hildrun	90	3.1459	0.1940	16.4752	62.54	5.55	0.052	0.013	-3.096	0.159	111
02621	Goto*	80	3.0922	0.1207	12.2630	47.92	5.64	0.080	0.034	-3.708	0.384	71
01113	Katja	90	3.1136	0.1324	13.7567	48.37	7.19	0.067	0.030	-2.027	0.229	51

Most of the families we identify here are analogous to those given by Nesvorný (2012), though we identify 28 new families above our significance threshold that were not previously known. In addition, 24 families from Nesvorný (2012) are lost in our analysis: fifteen fell below our cutoff size

Table 3: Orbital and physical parameters for Main Belt asteroids associated with dynamical families. Table 3 is published in its entirety in the electronic edition of ApJ; a portion is shown here for guidance regarding its form and content.

Name	a (AU)	ecc	inc (deg)	D (km)	σ_D	p_V	σ_{p_V}	Family
00004	2.3615	0.0988	6.3903	468.30	26.70	0.423	0.053	00004
00063	2.3952	0.1206	6.2173	109.51	2.25	0.142	0.022	00004
01273	2.3938	0.1226	6.2289	6.77	0.15	0.299	0.035	00004
01906	2.3736	0.0994	6.4076	8.06	0.08	0.228	0.047	00004
01929	2.3627	0.1141	7.0768	7.24	0.24	0.389	0.081	00004
01933	2.3530	0.0940	6.8229	5.48	0.07	0.454	0.044	00004
01959	2.3161	0.0945	6.8517	7.31	0.14	0.230	0.055	00004
01979	2.3740	0.1015	6.5229	4.52	0.16	0.357	0.030	00004
02011	2.3870	0.1113	6.3730	5.19	0.65	0.463	0.100	00004
02024	2.3254	0.0948	6.5575	8.64	0.22	0.180	0.016	00004

while nine no longer link at the QRL level when the albedo components are considered separately. We have cross-referenced the lists of family members for overlapping families in the high-confusion IMB region and removed duplicate objects in the larger family if they appear in the membership list of a smaller family to ensure that the small family does not drop below our cutoff. This resulted in objects being rejected from the Flora family list that were linked to Baptistina, and objects being rejected from the Hertha family list that appeared in the Polana list.

Figures 10 and 11 compare the orbital elements and albedos of objects identified as part of an asteroid family in this work to those parameters of the objects that were not linked to any family and thus assumed to be part of the background. In Figure 12 we separate each semimajor axis and albedo region and plot the eccentricities and inclinations of the identified families, while Figure 13 shows all background objects in the same fashion. We see in these plots evidence of halos in the background distributions around the locations of known large families, indicating an incomplete identification (and thus removal) of these families. For example, the background objects from the OMB_{high} region show a halo near $0 < ecc < 0.1$ and $8^\circ < inc < 13^\circ$ corresponding to unlinked Eos family members. These halos likely represent family members that could not be linked to the core of the family at the QRL for that region, possibly because they have diffused into the background population due to high initial ejection velocities, Yarkovsky drift, and/or gravitational perturbation. We note two features in the IMB: a number of low albedo objects from the Polana family have been dragged into the IMB_{high} by the Hertha family from the region of albedo overlap included in the high albedo cutoff; and the moderately-high albedo Baptistina family is plotted in the IMB_{low} region as this family blends with Flora and cannot be distinguished in the high albedo population.

As is clearly shown in these plots, careful fine-tuning of the cutoff velocity and extraction

of each individual family could increase the population of known families significantly. This is particularly true for the high inclination regions where spatial densities are low; using a single QRL for the high and low inclination components of each region is likely resulting in a failure to identify a large number of family members at high inclinations (e.g. near the Hungaria family at $a \sim 1.8$ AU, $inc \sim 20^\circ$, and $ecc \sim 0.08$). However, subdividing each region’s QRL and fine-tuning each family’s cutoff velocity increases the subjectivity of the family determination; future work will attempt to investigate this more quantitatively. It is likely that this extension to the present work will increase the fraction of the MBAs that are members of a family significantly, possibly to $\sim 50\%$ or more which would mean that most asteroids are by-products of a catastrophic collision or large cratering event (cf. Bottke *et al.* 2005).

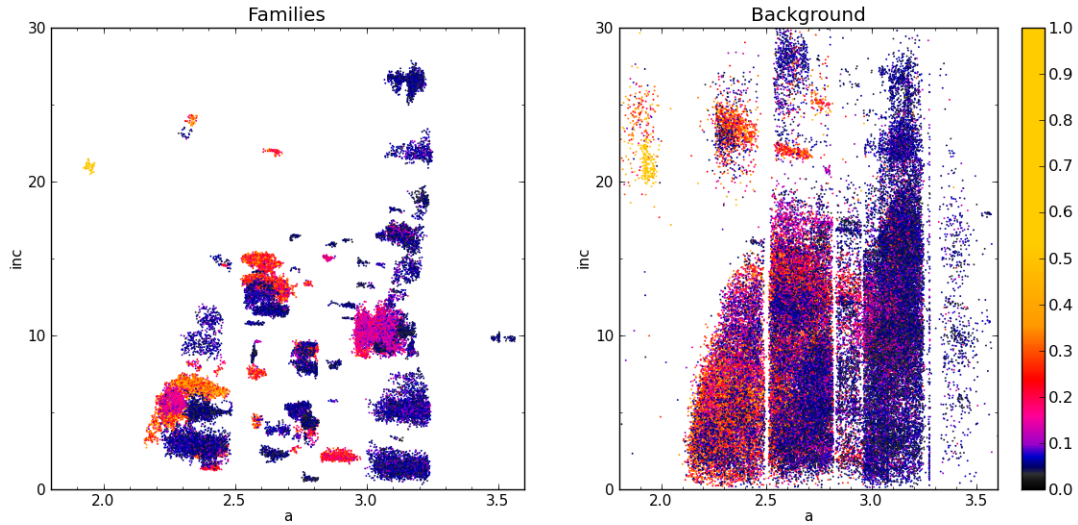


Fig. 10.— Proper inclination (inc , in degrees) vs. proper semimajor axis (a , in AU) for all identified family members (left) and all non-family background objects (right). The color of the points indicates the albedo of the asteroid as in Figure 1 and shown by the color bar.

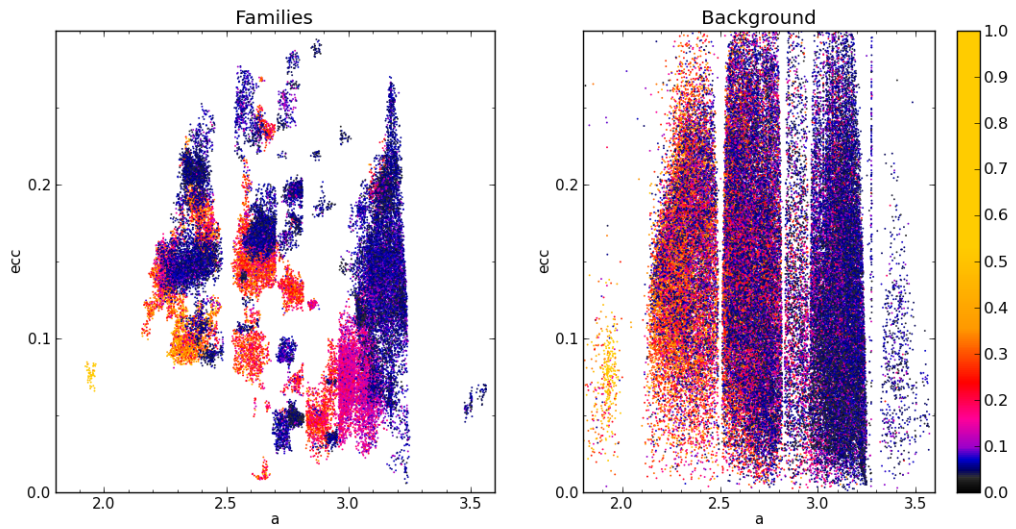


Fig. 11.— Proper eccentricity (ecc) vs. proper semimajor axis (a , in AU) for all identified family members (left) and all non-family background objects (right). The color of the points indicates the albedo of the asteroid as in Figure 1 and shown by the color bar.

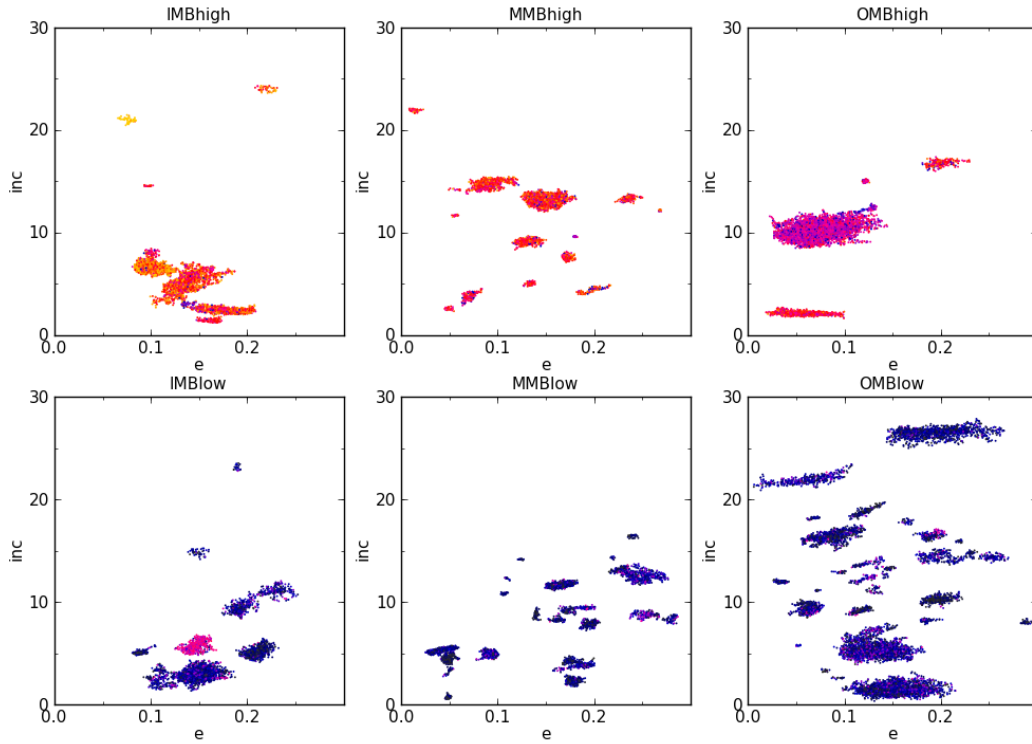


Fig. 12.— Proper inclination (inc , in degrees) vs proper eccentricity (ecc) for identified family members for each of the six semimajor axis and albedo regions considered in this work (see Table 1 for the definition of each region). Color indicates the albedo of the asteroid as in Figure 1.

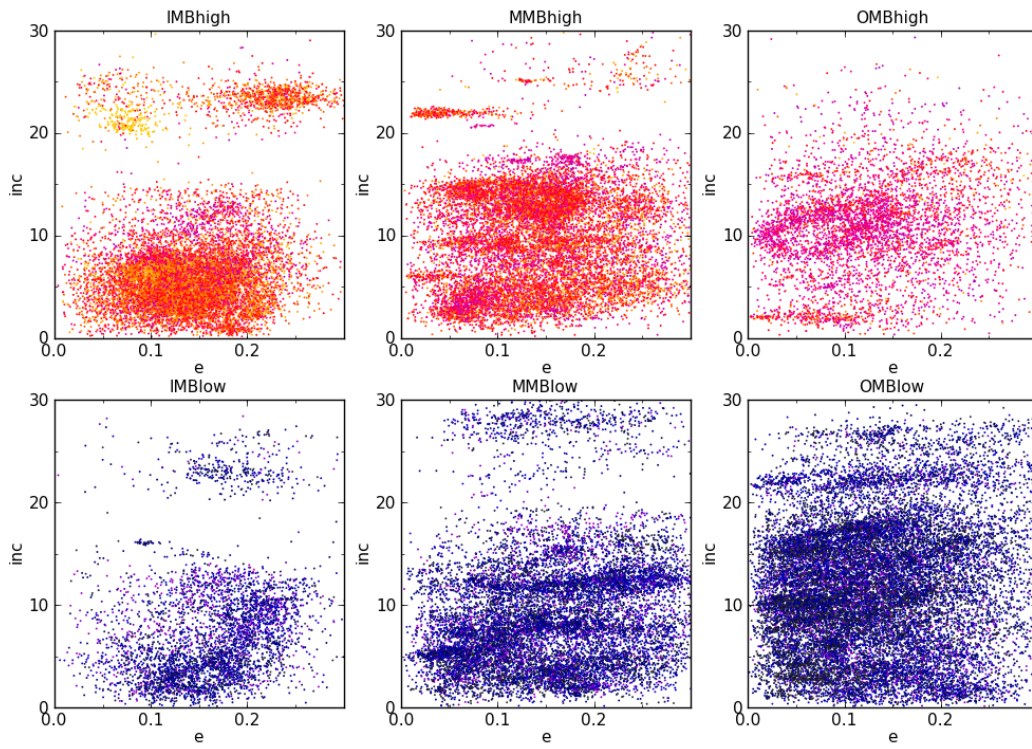


Fig. 13.— The same as Figure 12 but for background objects not part of any identified family.

Gil-Hutton (2006) identified 13 nominal families at high inclinations using proper orbital elements and HCM. Seven of those correspond to families that we identify here, one was linked by our routine but was too small to pass the reliability cuts. The remaining five found by Gil-Hutton (2006) were not linked in our method, however four of those had only a small number of members. In particular, we can not link any of the three families those authors identify in the IMB below our nominal QRL. We are also unable to identify any of the new families presented in (Novaković *et al.* 2011). These differences in family lists are a result of our application of a single QRL to both high and low inclination IMB objects despite the large differences in spatial density between the two populations. We anticipate that with further refinement of the QRL for high inclination objects these families will be recoverable.

Recently, Broz *et al.* (2013) published a revised list of asteroid family members, rerunning the HCM linking routine over the latest list of asteroids. The majority of the families those authors present are similar to the ones we discuss here, and most of their families we do not find are because they are too small, at high inclination, or do not link at our QRL when confusion with background sources is reduced. There are two specific examples of differences between this work and theirs that we comment on here. First, Broz *et al.* (2013) identify a family around (1044) Teutonia with 1950 members, however in our data this family does not link significantly at a level below our QRL, and at the QRL only links to ~ 65 objects. Second, they identify a family around (2085) Henan with 946 members, however as with Teutonia this family does not link below our QRL level. We interpret both of these cases as instances where confusion with background sources is eliminated when albedos are separated and thus linkages no longer become significant.

We compare in Figure 14 the albedo distribution of asteroids linked to a dynamical family to the distribution for background objects for each of the three orbital regions considered. While the family members show roughly equal contributions from high and low albedo objects in all three regions, the background objects show the opposite trend. The IMB background is dominated by the higher albedo component, while the OMB background has only a minimal contribution from these objects. This division is likely to become even more extreme once the halo objects are properly accounted for, as these make up a large fraction of the IMB_{low} and OMB_{high} objects remaining in the background population.

In Figures 15-20 we show the individual petal plots for each of the families we identify, separated into regions. Each subplot is labeled with the name of the largest body; names in blue font with a ‘*’ suffix indicate cases of ambiguous parent bodies, either because there is no clear largest body (e.g. Endymion) or there is a small group of objects of similar sizes that could be the parent or represent a completely shattered parent (e.g. the Eos family, where (221) Eos, (639) Latona, and (579) Sidonia are clustered at similar semimajor axes with diameters of $D= 96$ km, 89 km, and 86 km respectively). In some cases it is clear that the listed family likely represents two overlapping families (e.g. Emma). We also indicate Baptistina as an ambiguous case given the results found in Masiero *et al.* (2012b).

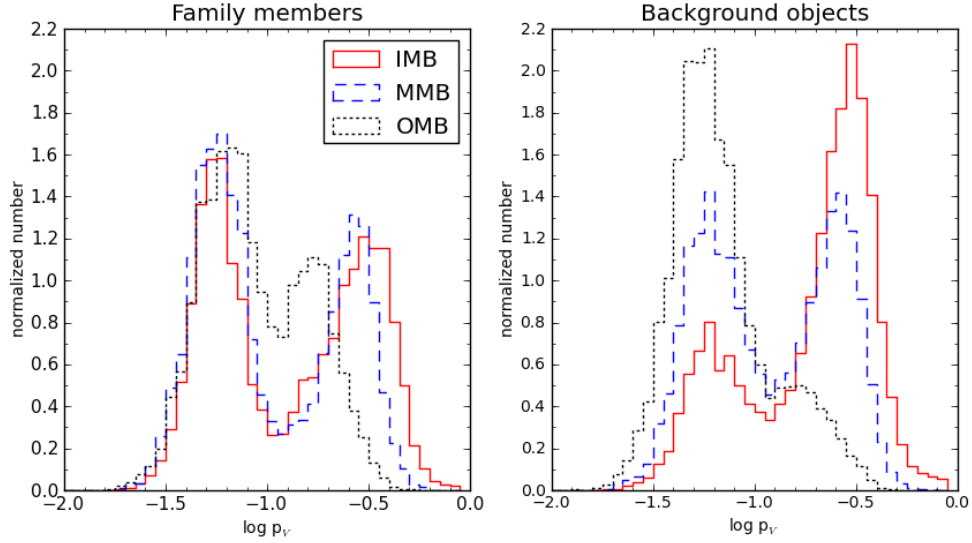


Fig. 14.— Albedo distribution for the IMB (red solid), MMB (blue dashed), and OMB (black dotted) for all identified family members (left) and all background objects (right)

We note that as we have chosen to identify families by the name of the largest member, rather than the lowest numbered object, in some cases well-known families have changed name. A prime example of this is the Lacrimosa family, which encompasses the well-known Koronis family. As (208) Lacrimosa has a larger diameter than (158) Koronis ($D = 50$ km vs $D = 39$ km) our naming system assigns the family to Lacrimosa, but this case is another example of a family with an ambiguous parent.

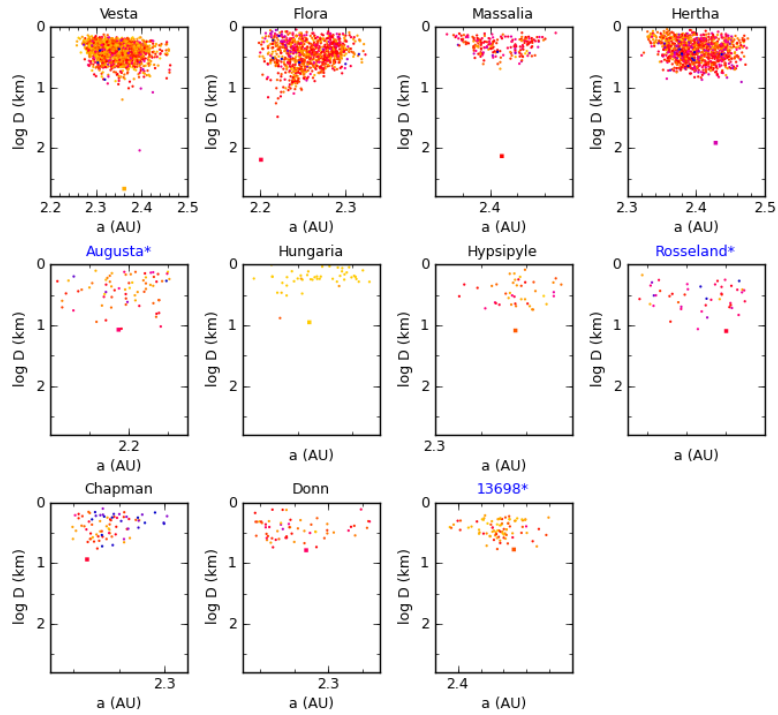


Fig. 15.— Diameter vs semimajor axis petal plots for all significant families in the high albedo inner Main Belt region. The parent body is indicated as the larger square point. Names with a ‘*’ suffix have ambiguous parent bodies. Colors of the points indicate the albedo of the asteroid as in Figure 1.

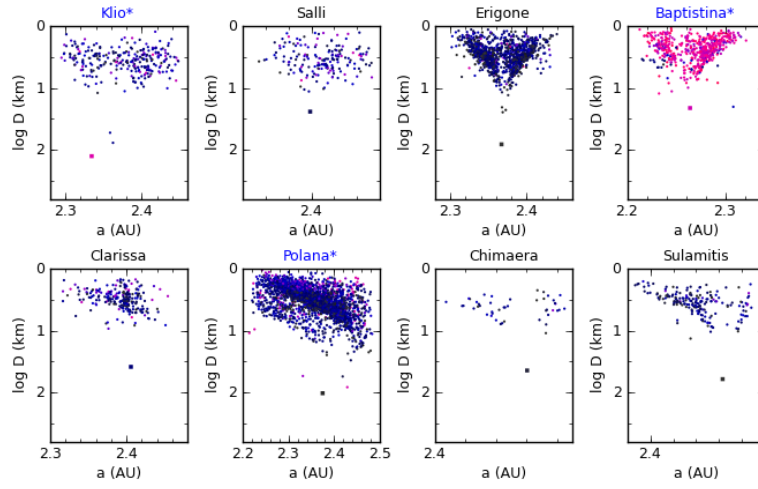


Fig. 16.— The same as Figure 15 but for the low albedo inner Main Belt.

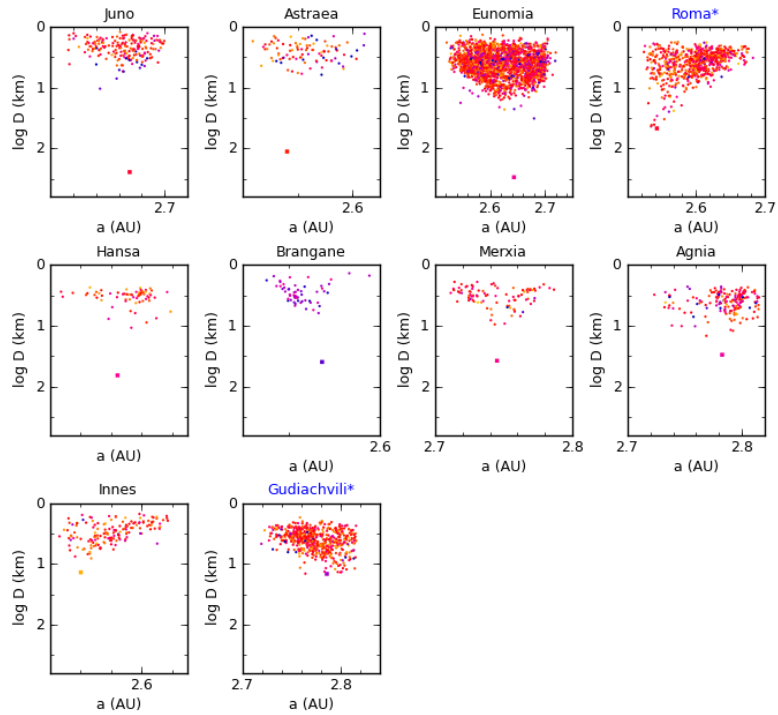


Fig. 17.— The same as Figure 15 but for the high albedo middle Main Belt.

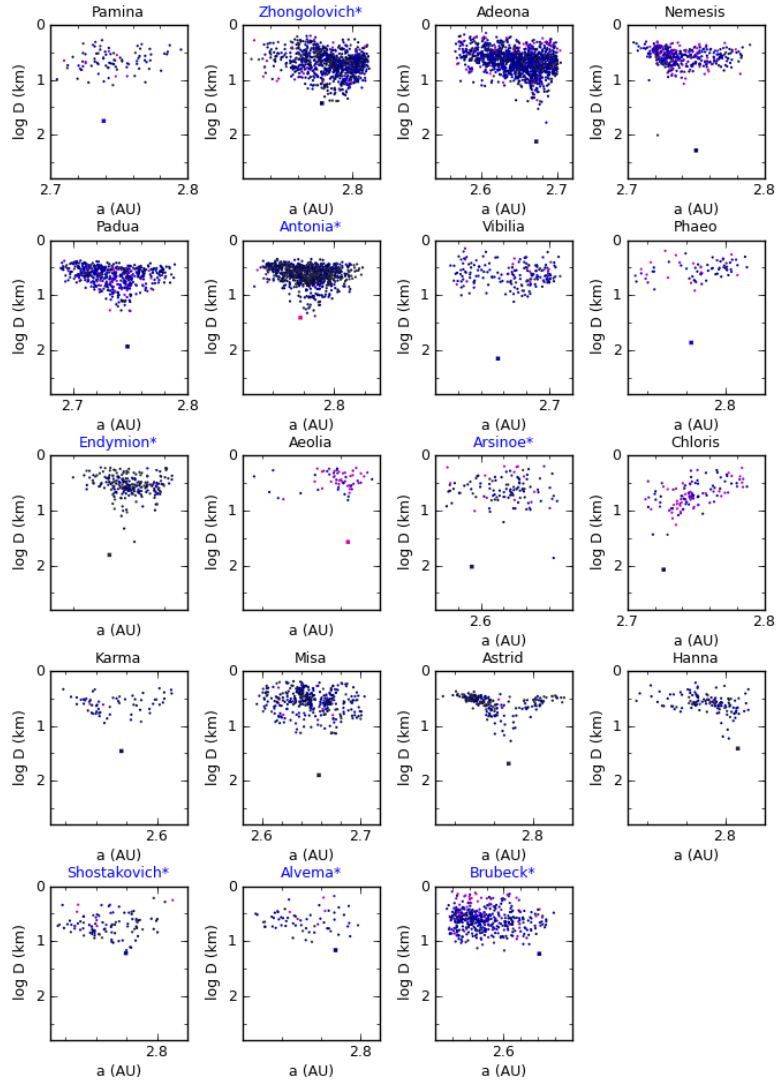


Fig. 18.— The same as Figure 15 but for the low albedo middle Main Belt.

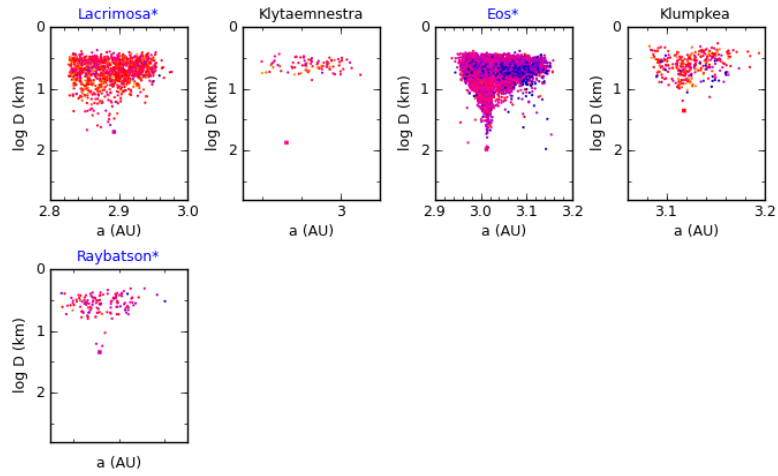


Fig. 19.— The same as Figure 15 but for the high albedo outer Main Belt.

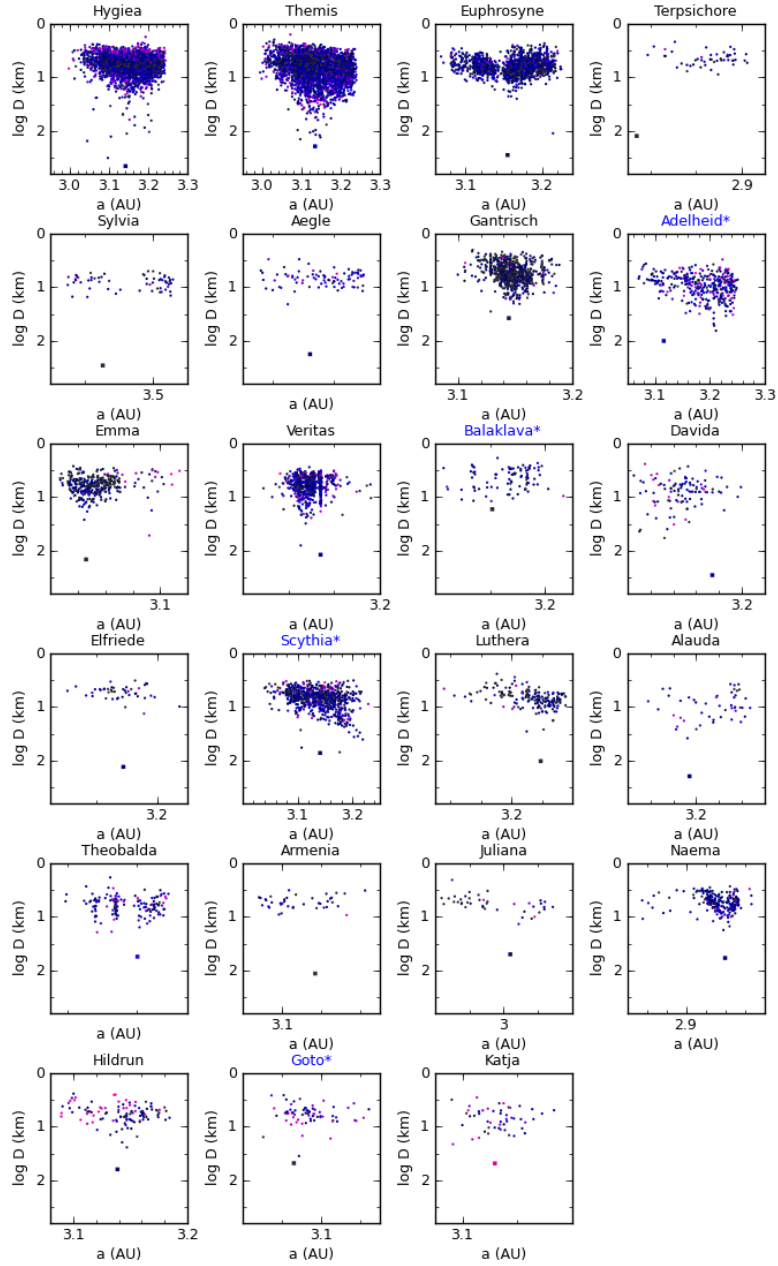


Fig. 20.— The same as Figure 15 but for the low albedo outer Main Belt.

4.2. Family Physical Properties

Using the high-confidence family lists we investigate the physical parameters of each family including the characteristic size, raw size-frequency distribution (SFD) and mean albedo as they relate to number of family members identified and size of the largest remnant. We note that as shown in Figure 1 our sample, limited by the biases imposed predominantly by visual band detection, is not complete to the same sizes for high- and low-albedo objects. This means that the minimum and median sizes of low albedo families will be shifted to larger values than for high albedo families. Additionally, for a given family the wing of the albedo distribution at higher values will be better sampled than the wing at lower values. Also note that our imposed division of albedos into two components will remove objects that have albedos very different from the bulk of the family due to incorrect measurements or large physical differences. These biases will affect the measurement of SFD as well, so care in interpretation is required.

We present the observed cumulative size distribution for each family in Figure 21, and the differential albedo distribution for each family in Figure 22. Approximately two-thirds of the families show a single parent body much larger than the remaining members, while the remaining families do not show a dominant remnant. This may be indicative of differences between cratering events and super-catastrophic disruptions as discussed by Durda *et al.* (2007), however in the latter families we cannot rule out cases where the largest remnant is present but did not link to the family due to the various cutoffs imposed. As opposed to what was seen in Mas11, where $\sim 25\%$ of the previously published families had non-uniform albedo distributions, almost none of the families presented here show any bimodality in their albedo distributions. The few exceptions (e.g. Chapman, Astraea) are expected to be artifacts that will be removed with future planned revisions of the family selection cutoffs. Given our separation of the regions into high- and low-albedo components, this result is not unexpected.

Using these distributions, we can determine initial physical properties for each family with the caveat that selection biases imposed by visible light surveys have not yet been removed and so will bias our results as well. We fit a Gaussian profile to the albedo distribution of each family to derive the mean albedo (p_V) and Gaussian width (σ_{p_V}), which is 20% – 30% of the mean for nearly all of the families we observe. This width is comparable to the uncertainty we expect in the albedo determination from the NEOWISE data (Mas11, Mainzer *et al.* 2011b). Using the diameter distribution, we can size-sort the linked family to find the diameter of the largest body (D_{max}), the median diameter of the observed sample (D_{med}), as well an initial estimate of the observed, raw SFD.

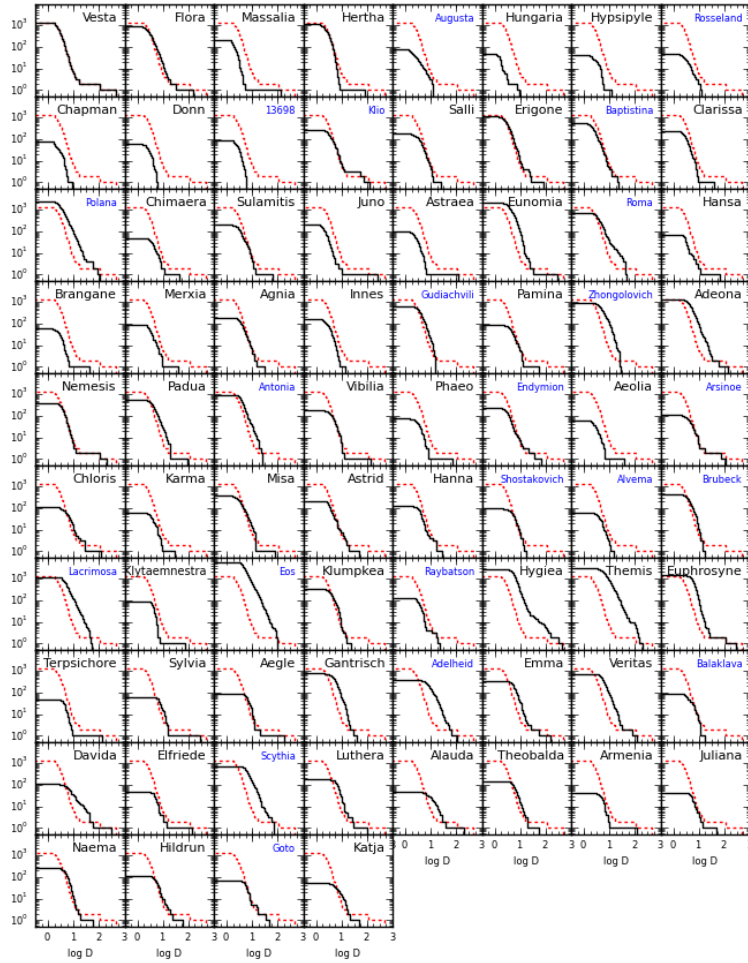


Fig. 21.— Cumulative raw size distribution of family members identified in this study for the 76 families presented in Table 2. The red dashed line shows the distribution for the Vesta family, for comparison. Family names in blue indicate cases where the parent body is uncertain. As discussed in the text, selection biases from visible light surveys have not been quantified which will affect interpretation of these distributions.

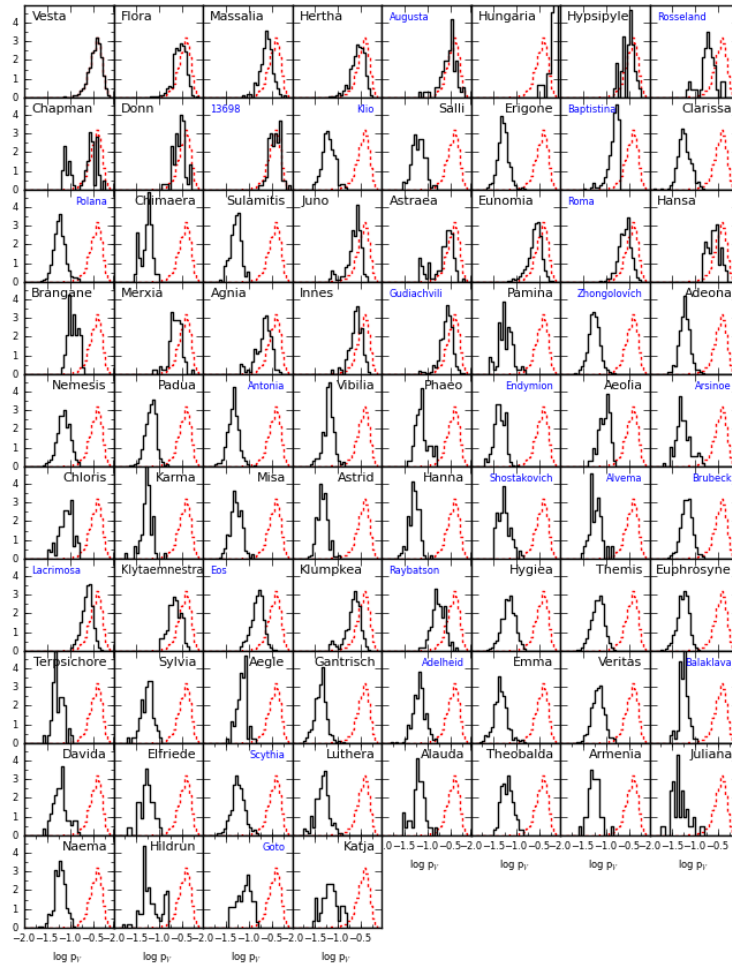


Fig. 22.— Differential raw distribution of albedos for the 76 families presented in Table 2. The red dashed line shows the distribution for the Vesta family, for comparison. Family names in blue indicate cases where the parent body is uncertain. As discussed in the text, selection biases from visible light surveys have not been quantified which will affect interpretation of these distributions.

To determine the observed SFD we fit a function of $N = D^\alpha$ to each cumulative distribution, using only those bins with more than five objects (to avoid errors induced by a few large fragments in a cratering scenario) and less than half of the sample (to minimize errors due to the incomplete catalogs). Using a least-squares minimizer we derive the best-fit slope parameter (α_{SFD}) and the 1σ error on that slope (σ_α). We see in our sample a range of slope parameters, from $\alpha \sim -1.5$ at the shallowest to $\alpha \sim -5$ at the steepest. SFD slope can be used to study the conditions of the breakup event (e.g. the curve of the SFD can trace cratering vs. catastrophic disruption, Durda *et al.* 2007), however these slopes can be modified over time as collisional grinding alters the initial post-breakup population, flattening the SFD over time (Marzari *et al.* 1995). Additionally, if the parent body prior to impact had a shattered interior structure, this will also change the expected SFD of the family by increasing the frequency of reaccumulation of large family members (Michel *et al.* 2004).

The specific bins chosen for fitting will alter the fitted slope depending on the shape of the SFD. Tests on our data show that varying the lower limit over a range from five to fifty objects typically causes the fitted slopes to become shallower by $\Delta\alpha \sim 0.1 - 0.3$, with the effect becoming more pronounced for smaller families as the sample size decreases. This indicates that most families have steeper size distributions in the biggest objects than in the majority of the population, however this is probably at least partially a result of survey incompleteness at smaller diameters. Conversely, when we test the effect of changing the upper limit for fitting from half the population down to only the largest 25%, we see that the fitted slopes generally move away from a value of $\alpha \sim -2.5$ as fewer objects are included in the fit (cf. Tanga *et al.* 1999). This shift is typically $\Delta\alpha < 0.5$ however for the most extreme case (the Hertha family) it is as large as $\Delta\alpha = 1.3$. As most families have measured slopes of $\alpha < -2.5$ this means that their SFDs become steeper as objects are removed. This effect may also be a result of survey incompleteness at the smallest sizes, or may be tracing either a collisional equilibrium at smaller sizes with the background population which has $\alpha \sim -2.5$ (Mas11) or an increasing fraction of non-family members being included in family lists at these sizes.

This uncertainty in the fit to the observed SFD is compounded by the visible-light survey biases that are incorporated into the optical measurements we use to determine albedo. Objects without albedos do not pass our initial cuts for inclusion into our data set, thus our sample will include some effect from these biases, which will be particularly pronounced for smaller, lower albedo objects. These biases will result in systematic and potentially large errors in the fits to the observed SFD. Debiasing of the MBA background and family populations is critical to measuring the true SFDs and physical parameters for asteroid families, and as such values given here should be regarded as preliminary.

We present in Table 2 the determined albedo, diameter, and slope parameters for each of the 76 significant families we identify. These values are subject to large biases due to incomplete sampling of various subpopulations within the MBAs, so care in interpretation is required. We note that as families indicated by a ‘*’ suffix on their name have ambiguous parent bodies, the size of the

largest linked object is not necessarily indicative of the size of the parent or largest remnant.

We show in Figure 23 a comparison of the mean family albedo to the median diameter. As expected from the biases against smaller, lower albedo objects imposed by visible light surveys used to create the catalog our sample is drawn from, high albedo families have a smaller median diameter than low albedo families. Despite this bias, nearly two-thirds of the observed families are low albedo. As catalogs of asteroids become more complete at small sizes for low albedo objects we expect that the number of low albedo families identified will increase further. We also see indications for four distinct albedo classes in the families: low albedo ($p_V \sim 0.06$), moderate albedo ($p_V \sim 0.16$), high albedo ($p_V \sim 0.25$) and the very high albedo Hungaria family ($p_V > 0.40$). We note that while updates to the measured magnitudes of the Hungaria family including better fits of H and G are expected to reduce the H magnitudes and thus the determined albedos (B. Warner, 2012, private communication), these family members still typically have $p_V > 0.40$ and are expected to remain narrowly distributed.

If we take albedo as a coarse tracer of the parent body’s composition (cf. Mainzer *et al.* 2011c) we can search for any influence this has on the resultant breakup. We show in Figure 24 a comparison between the characteristic family albedo and the fitted observed SFD slope. If different compositions traced different cohesion strengths, we would expect to see a correlation between these two parameters, however we see no such relationship. This may indicate that albedo does not correlate with internal structure, or that impact geometry and/or energy play the dominant role in shaping the SFD of the family, as shown by Durda *et al.* (2007), however debiasing must be performed before definite conclusions can be drawn.

Figure 25 shows the comparison between the observed raw SFD slope and the size of the linked family. Clearly, families with smaller numbers of objects will have more uncertain SFD slopes. However, there does appear to be a trend toward shallower slopes for larger families. We note that in a diameter-limited survey such as NEOWISE fewer objects are expected to link to families with steep SFDs than shallow SFDs, as a larger fraction of the family members will be at or below the survey detection threshold. This may be a contributing factor to the lack of large, steep SFD families. Conversely, biases due to variable survey completeness can induce systematic errors. As steep families are thought to be young, and a large family indicates an energetic collision, these families are expected to be rare, confusing any interpretation of their absence. A survey probing a smaller size range would preferentially fill in the membership lists of steep SFD families allowing better measurements of their SFDs to be made.

Tanga *et al.* (1999) and Durda *et al.* (2007) showed that steeper slopes tend to indicate families that originated from a cratering event, while shallower slopes tend to follow disruptive impacts. This suggests that in the diameter range we are sensitive to, most of the numerically largest families in the Main Belt formed from disruptive events. An exception to this trend is the (31) Euphrosyne family, which has ~ 1400 members but one of the steepest slopes measured with $\alpha_{SFD} = -4.4$. This unusually steep observed SFD may be indicative of a glancing impact between two large bodies

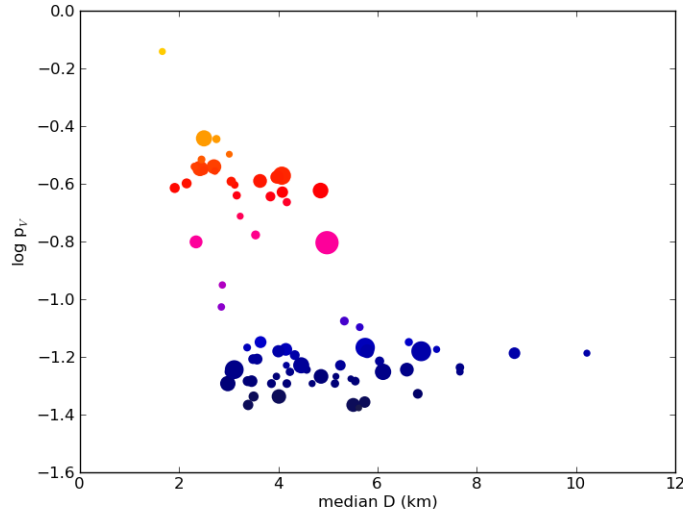


Fig. 23.— Characteristic albedo for each family compared to the median diameter of all objects linked to that family. The size of the points indicates the number of objects in the family, while the color also traces albedo, following Figure 1. As expected, higher albedo families have small median diameters as selection effects against smaller, lower albedo asteroids imposed by visible light surveys have not been removed.

resulting in a large cratering event. We note that this observed SFD is significantly steeper than what is observed for (4) Vesta ($\alpha = -3.45$, the next steepest SFD in this family size range), which is known to have undergone two massive cratering events from the results of the Dawn mission (Russell *et al.* 2012). Conversely, the observed SFD of the Euphrosyne family may trace a low-speed collision where reaccumulation onto the parent was highly efficient. In this scenario only those objects with the highest ejection velocities, preferentially the smallest ejecta, would fail to reaccrete and would become independent family members. As grazing impacts have a much lower frequency of binary production than slower, head-on impacts (Durda *et al.* 2004), a search for binaries in the Euphrosyne family could differentiate between these two scenarios. However, until proper debiasing of the MBA population is complete and debiased SFDs can be measured, these possible formation scenarios are speculative.

5. Conclusions

In order to identify new asteroid families and improve the lists of previously known families, we have used the databases of asteroid diameters and albedos provided by the WISE/NEOWISE and IRAS surveys as a method of incorporating asteroid physical properties into family determination.

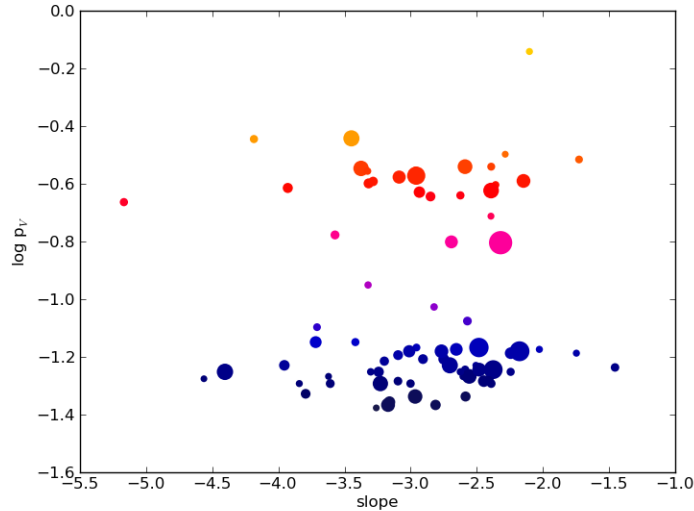


Fig. 24.— The same as Figure 23, now showing albedo vs. SFD slope parameter. For the largest families the error on the slope fit is smaller than the size of the point, however systematic errors due to survey bias have not been included.

After splitting the MBAs into two separate but overlapping albedo populations and three orbital regions, we have applied the Hierarchical Clustering Method to these subgroups. This technique is particularly useful for rejecting interlopers from family lists, including objects that would otherwise be misidentified as the family’s largest remnant. We identify 76 families with more than 40 members in our high-confidence set, of which 28 were previously unreported. One third of these families do not have an obvious parent asteroid that links to the family. Approximately 35% of MBAs link into a family, however there are clear limitations to our method apparent at high inclinations and in crowded regions. Carefully tuned family extraction will likely increase this percentage significantly.

The observed albedo distribution of the 38,298 identified family members differs significantly from the distribution of the background asteroids, where the background shows a more extreme change from the inner- to outer-Main Belt. We see no correlation between the slope of the observed, raw size frequency distribution of a family and its mean albedo. However, we note that a full accounting for the selection biases imposed by the visible light surveys that discovered the objects has not yet been performed, and an unquantified number of objects are thus missing from each family; these biases must be accounted for before firm conclusions about the SFDs for each family can be made. Of the observed raw SFDs, we note a trend that families with larger numbers of objects tend to have more shallow slopes. One possible explanation is that these families were created could by catastrophic disruption or are very old and have been ground down by collisional processing over very long timescales. An exception to this trend is the (31) Euphrosyne family

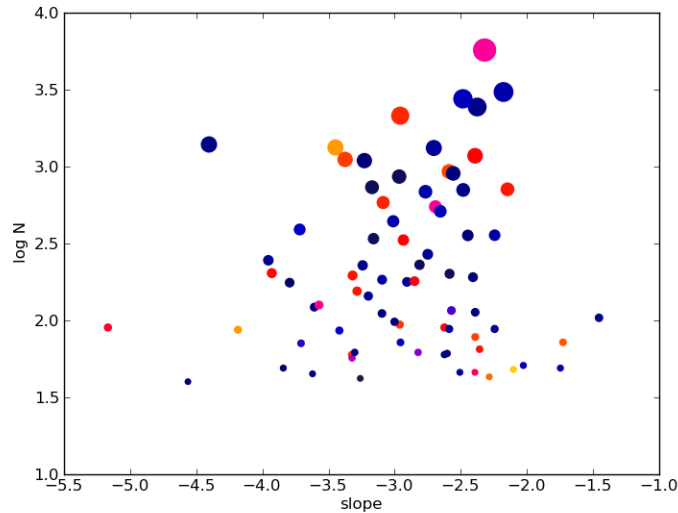


Fig. 25.— The same as Figure 23, now showing size of the linked family vs. observed raw SFD slope parameter. For the largest families the error on the slope is smaller than the size of the point, however systematic errors due to survey bias have not been included.

which has one of the steepest size frequency distributions measured, but is also one of the largest families observed. This could be the result of a cratering impact between two large bodies, a recent giant impact, or both. While this work only includes approximately one quarter of the known MBA population (those observed by NEOWISE and IRAS), it sets the stage for improving our understanding of the creation and evolution of MBA families. Future work will improve our family identification routines to better differentiate family members from background objects and debias the input catalog, improving our family lists and setting the stage for the determination of ages for the majority of families in the Main Belt.

Acknowledgments

JM was partially supported by an appointment to the NASA Postdoctoral Program at JPL, administered by Oak Ridge Associated Universities through a contract with NASA. The authors thank the referee Alberto Cellino for comments that greatly improved the paper, and John Dailey for helpful discussions on implementation of algorithms. This publication makes use of data products from the Wide-field Infrared Survey Explorer, which is a joint project of the University of California, Los Angeles, and the Jet Propulsion Laboratory/California Institute of Technology, funded by the National Aeronautics and Space Administration. This publication also makes use of data products from NEOWISE, which is a project of the Jet Propulsion Laboratory/California Institute

of Technology, funded by the Planetary Science Division of the National Aeronautics and Space Administration. This research has made use of the NASA/IPAC Infrared Science Archive, which is operated by the Jet Propulsion Laboratory, California Institute of Technology, under contract with the National Aeronautics and Space Administration. We gratefully acknowledge the extraordinary services specific to NEOWISE contributed by the International Astronomical Union’s Minor Planet Center, operated by the Harvard-Smithsonian Center for Astrophysics, and the Central Bureau for Astronomical Telegrams, operated by Harvard University.

REFERENCES

- Bendjoya, Ph. & Zappalà, V., 2002, Asteroids III, W. F. Bottke Jr., A. Cellino, P. Paolicchi, and R. P. Binzel (eds), University of Arizona Press, 613.
- Binzel, R.P. & Xu, S., 1993, *Science*, 260, 186.
- Bottke, W.F., Durda, D.D., Nesvorný, D., *et al.*, 2005, *Icarus*, 175, 111.
- Bottke, W.F., Vokrouhlický, D., Rubincam, D.P. & Nesvorný, D., 2006, *AREPS*, 34, 157.
- Broz, M., Morbidelli, A., Bottke, W.F., Rozehnal, J., Vokrouhlický & D., Nesvorný, D., 2013, *A&A*, 551, A117
- Carpino, M., Gonczi, R., Farinella, P., Froeschle, Ch., Froeschle, Cl., Paolicchi, P. & Zappala, V., 1986, *Icarus*, 68, 55.
- Cellino, A., Zappalà, V., Doressoundiram, A., di Martino, M., Bendjoya, Ph., Dotto, E. & Migliorini, F., 2001, *Icarus*, 152, 225.
- Cellino, A., Dell’Oro, A. & Tedesco, E.F., 2009, *P&SS*, 57, 173.
- Durda, D.D., Bottke, W.F., Enke, B.L., *et al.*, 2004, *Icarus*, 167, 382.
- Durda, D.D., Bottke, W.F., Nesvorný, D., *et al.*, 2007, *Icarus*, 186, 498.
- Gil-Hutton, R., 2006, *Icarus*, 183, 93.
- Grav, T., Mainzer, A., Bauer, J., *et al.*, 2011a, *ApJ*, 742, 40.
- Grav, T., Mainzer, A., Bauer, J., *et al.*, 2011b, *ApJ*, 744, 197.
- Hirayama, K., 1918, *AJ*, 31, 185.
- Ivezić, Ž., Lupton, R.H., Jurić, M., Tabachnik, S., Quinn, T., Gunn, J.E., Knapp, G.R., Rockosi, C.M. & Brinkmann, J., 2002, *AJ*, 124, 2943.
- Knežević, Z. & Milani, A., 2000, *CeMDA*, 78, 17.
- Mainzer, A.K., Bauer, J.M., Grav, T., Masiero, J., Cutri, R.M., Dailey, J., Eisenhardt, P., McMillan, R.M. *et al.*, 2011a, *ApJ*, 731, 53.
- Mainzer, A.K., Grav, T., Masiero, J., Bauer, J.M., Wright, E., Cutri, R.M., McMillan, R.S., Cohen, M., Ressler, M., Eisenhardt, P., 2011b, *ApJ*, 736, 100.
- Mainzer, A.K., Grav, T., Masiero, J., *et al.*, 2011c, *ApJ*, 741, 90.
- Mainzer, A., Grav, T., Bauer, J.M., Masiero, J., *et al.*, 2011d, *ApJ*, 743, 156.

- Mainzer, A.K., Grav, T., Masiero, J., Bauer, J.M., Cutri, R.M., McMillan, R.S., Nugent, C., Tholen, D., Walker, R. & Wright, E.L., 2012, *ApJL*, 760, 12.
- Marzari, F., Davis, D. & Vanzani, V., 1995, *Icarus*, 113, 168.
- Masiero, J.R., Mainzer, A.K., Grav, T., Bauer, J.M., Cutri, R.M., Dailey, J., Eisenhardt, P.R.M., *et al.*, 2011, *ApJ*, 741, 68.
- Masiero, J.R., Mainzer, A.K., Grav, T., Bauer, J.M., Cutri, R., Nugent, C. & Cabrera, M.S., 2012, *ApJ*, 759, L8.
- Masiero, J.R., Mainzer, A.K., Grav, T., Bauer, J.M. & Jedicke, R., 2012, *ApJ*, 759, 14.
- Michel, P., Benz, W. & Richardson, D.C., 2004, *Icarus*, 168, 420.
- Milani, A. & Knežević, Z., 1994, *Icarus*, 107, 219.
- Milani, A. & Knežević, Z., 1998, *Celestial Mech. and Dynamical Astron.*, 71, 55.
- Milani, A., Knežević, Z., Novaković, B., & Cellino, A., 2010, *Icarus*, 207, 769.
- Muironen, K., Belskaya, I.N., Cellino, A., Delbò, M., Levasseur-Regourd, A.-C., Penttilä, A. & Tedesco, E.F., 2010, *Icarus*, 209, 542.
- Nesvorný, D., 2012, EAR-A-VARGBDET-5-NESVORNYFAM-V2.0, NASA Planetary Data System.
- Novaković, B., Cellino, A., & Knežević, Z., 2011, *Icarus*, 216, 69.
- Parker, A., Ivezić, Ž., Jurić, M., Lupton, R.H., Sekora, M.D. & Kowalski, A., 2008, *Icarus*, 198, 138.
- Pravec, P., Harris, A.W., Kušnirák, P., Galád, A. & Hornoch, K., 2012, *Icarus*, 221, 365.
- Reddy, V., Nathues, A., Le Corre, L., *et al.*, 2012, *Science*, 336, 700.
- Russell, C.T., Raymond, C.A., Coradini, A., *et al.*, 2012, *Science*, 336, 684.
- Tanga, P., Cellino, A., Michel, P., Zappalà, V., Paolicchi, P. & Dell’Oro, A., 1999, *Icarus*, 141, 65.
- Tedesco, E.F., Noah, P.V., Noah, M. & Price, S.D., 2002, *AJ*, 123, 1056.
- Wright, E.L., Eisenhardt, P., Mainzer, A.K., Ressler, M.E., Cutri, R.M., Jarrett, T., Kirkpatrick, J.D., Padgett, D., *et al.*, 2010, *AJ*, 140, 1868.
- Zappalà, V., Cellino, A., Farinella, P. & Knežević, Z., 1990, *AJ*, 100, 2030.
- Zappalà, V., Cellino, A., Farinella, P. & Milani, A., 1994, *AJ*, 107, 772.

Zappalà, V., Bendjoya, Ph., Cellino, A., Farinella, P. & Froeschle, C., 1995, *Icarus*, 116, 291.

Zappalà, V., Cellino, A., Dell’Oro, A. & Paolicchi, P., 2002, *Asteroids III*, W. F. Bottke Jr., A. Cellino, P. Paolicchi, and R. P. Binzel (eds), University of Arizona Press, 619.